journal of the mechanical behavior of biomedical materials 143 (2023) 105921

Contents lists available at ScienceDirect

Journal of the Mechanical Behavior of Biomedical Materials

journal homepage: www.elsevier.com/locate/jmbbm

Research paper

Mechanical loading of the ventricular wall as a spatial indicator for periventricular white matter degeneration

Valery L. Visser [a,b,1], Andreia Caçoilo [a], Henry Rusinek [c], Johannes Weickenmeier [a,*]

[a] Department of Mechanical Engineering, Stevens Institute of Technology, Hoboken, NJ 07030, United States of America
[b] Department of Biomedical Engineering, Eindhoven University of Technology, 5600 MB Eindhoven, The Netherlands
[c] Department of Radiology, New York University Grossman School of Medicine, New York, NY 10016, United States of America

ARTICLE INFO

Keywords:
White matter hyperintensities
Ependymal cells
Lateral ventricles
Finite element simulations
Tissue damage

ABSTRACT

Progressive white matter degeneration in periventricular and deep white matter regions appears as white matter hyperintensities (WMH) on MRI scans. To date, periventricular WMHs are often associated with vascular dysfunction. Here, we demonstrate that ventricular inflation resulting from cerebral atrophy and hemodynamic pulsation with every heartbeat leads to a mechanical loading state of periventricular tissues that significantly affects the ventricular wall. Specifically, we present a physics-based modeling approach that provides a rationale for ependymal cell involvement in periventricular WMH formation. Building on eight previously created 2D finite element brain models, we introduce novel mechanomarkers for ependymal cell loading and geometric measures that characterize lateral ventricular shape. We show that our novel mechanomarkers, such as maximum ependymal cell deformations and maximum curvature of the ventricular wall, spatially overlap with periventricular WMH locations and are sensitive predictors for WMH formation. We also explore the role of the septum pellucidum in mitigating mechanical loading of the ventricular wall by constraining the radial expansion of the lateral ventricles during loading. Our models consistently show that ependymal cells are stretched thin only in the horns of the ventricles irrespective of ventricular shape. We therefore pose that periventricular WMH etiology is strongly linked to the deterioration of the over-stretched ventricular wall resulting in CSF leakage into periventricular white matter. Subsequent secondary damage mechanisms, including vascular degeneration, exacerbate lesion formation and lead to progressive growth into deep white matter regions.

1. Introduction

White matter hyperintensities (WMH) are frequently observed on magnetic resonance images of the aging brain and are indicative of increased interstitial fluid content that is often related to white matter damage (Fazekas et al., 1993; Wardlaw et al., 2015). The association of WMHs with cognitive decline and their widespread prevalence in the aging population warrants a better understanding of the mechanisms contributing to WMH onset and subsequent growth (Debette and Markus, 2010; Maillard et al., 2014). Diffusion-based imaging has identified a myriad of microstructural changes associated with WMHs that point towards a complex etiology (Maillard et al., 2013). WMHs are predominantly thought to originate from vascular degeneration or white matter lesions (Blinkouskaya and Weickenmeier, 2021). They are attributed to cerebrovascular small vessel diseases (Wardlaw et al., 2015, 2003; Lambert et al., 2016; Fernando et al., 2006) and exacerbated in severity by risk factors such as hypertension (Cheng et al., 2018; Gouw et al., 2008), smoking (Fukuda and Kitani, 1996; Kim et al., 2012), diabetes (Al-Anbari et al., 2020; Nunley et al., 2015), and heart disease (Lee et al., 2018; Gouw et al., 2008). WMHs are typically classified based on their location as either deep WMHs (dWMHs) or periventricular WMHs (pvWMHs) despite continued debate about their primary disease mechanisms (Mayer and Kier, 1991; Jung et al., 2021). There is growing recognition that dWMHs and pvWMH have different etiology (Fazekas and Wardlaw, 2013; Armstrong et al., 2020). Pathology-based studies have reported extensive ependymal cell damage, astrogliosis, and CSF leakage into periventricular tissues in locations associated with pvWMHs (Shook et al., 2014; Jiménez et al., 2014; Roales-Buján et al., 2012; Scheltens et al., 1995).

As highlighted in Fig. 1, pvWMHs first appear as thin bright linings in FLAIR imaging, then progress to caps, and ultimately appear as diffuse bright regions penetrating into deeper white matter tissue (Fazekas et al., 1987). This gradual involvement of deeper white matter tissues

* Corresponding author.
E-mail address: johannes.weickenmeier@stevens.edu (J. Weickenmeier).
[1] Current address: Institute for Regenerative Medicine, University of Zurich , 8006 Zurich, Switzerland.

https://doi.org/10.1016/j.jmbbm.2023.105921
Received 21 February 2023; Received in revised form 15 May 2023; Accepted 18 May 2023
Available online 24 May 2023

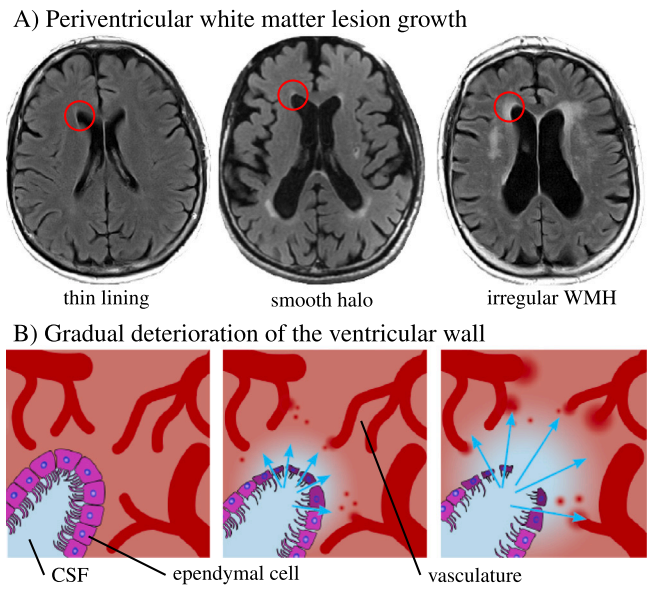

Fig. 1. (A) Periventricular white matter lesions gradually deteriorate from thin linings to smooth halos and eventually spread into deep periventricular white matter tissue. (B) Hypothesized corresponding stages of ependyma damage in a horn of the lateral ventricles; starting from an intact ependyma with proper barrier function, propagating to loss of barrier function and increased CSF diffusion into the white matter, ultimately leading to severe white matter and cerebrovascular damage. Ependymal cells, shown in purple, are not to scale; CSF is shown in blue and parenchyma in orange.

suggests that damage originates at the highly functional barrier lining the ventricular wall and gradually triggers secondary white matter damage mechanisms. Anatomically, the ventricular wall consists of four layers (Quiñones-Hinojosa et al., 2006). The first layer is made of polarized ciliated cuboidal ependymal cells that are tightly connected with gap junctions, or desmosomes. The ependyma regulates nutrient and fluid exchange between parenchyma and ventricle (Oliver et al., 2013; Veeraval et al., 2020; Bruni et al., 1985). The second, hypocellular layer, is made up of processes from ependymal cells and astrocytes, the third layer is formed by a densely packed ribbon of astrocytes, and the fourth layer marks a transitional zone into the brain parenchyma (Del Bigio, 2009). Based on work by Quiñones-Hinojosa et al. (2006), we estimate the mean thickness of layers I-III of the ventricle's main body to be 11.0 ± 2.6 μm, 18 ± 4.6 μm, and 69.0 ± 2.0 μm, respectively.

Because the ventricular wall experiences high mechanical loads, it is prone to damage (Pena et al., 1999; Zhou et al., 2020). Brain aging-related cerebral atrophy and corresponding ventricular enlargement create progressively increasing strains on periventricular tissues and the ventricular wall (Blinkouskaya and Weickenmeier, 2021). On top of that, hemodynamic loading from every heartbeat causes cyclic expansion of periventricular tissues and contributes to atrophy-related ependymal cell strains (Terem et al., 2018). We pose that pvWMHs are tightly linked to mechanical damage in predictable locations along the ventricular wall. Subsequent loss of the ventricular wall's semipermeable barrier function and CSF accumulation in periventricular tissues causes secondary damage mechanisms including inflammation, demyelination, and axon damage which are clearly visible on diffusion-based images (Van Leijsen et al., 2018; Maniega et al., 2015; De Groot et al., 2013).

In previous works, we used computational modeling to show that maximum ependymal cell stretch, a prerequisite for wall failure, coincides with pvWMH locations for both anatomically accurate 2D and 3D brain models (Visser et al., 2021; Caçoilo et al., 2022). We selected eight subjects, four female and four male subjects, from a broad range of ventricular volumes to demonstrate that maximum mechanical loading consistently localizes in the ventricular horns and along the edges of the ventricle's main body. Our models predicted the response of periventricular tissue at peak hemodynamic loading. Arterial pulsations drive the oscillatory flow of CSF and causes lateral ventricles to cyclically expand and contract (Abderezaei et al., 2020). We reproduced the corresponding mechanical loading state at peak hemodynamic pressure, by applying a quasi-static pressure to the ventricular surface that induces wall deformations observed in vivo (Abderezaei et al., 2020). We found that ependymal cells were consistently stretched most along the edge of the ventricle's main body and in the anterior and posterior horns than any other location along the ventricular wall. For all of our eight subject's these locations also exhibited pvWMHs. Our findings were independent of ventricular volume and applied to a broad range of ventricular shapes.

Recently, we introduced ventricular horn radius, i.e. the individual radii of circles that approximate the ventricle's anterior and posterior horns in the axial slice with the largest ventricular area, as a reliable predictor for increased ventricular wall loading and pvWMH locations (Visser et al., 2021). The objective of the present study is to use our 2D models to further evaluate the mechanical loading state along the ventricular wall and its implications on the ependymal cells that form this highly relevant functional brain-fluid barrier. We introduce additional mechanomarkers to substantiate our proposed periventricular white matter damage mechanism. Specifically, we pose that curvature of the ventricular wall and ependymal cell stretches are good spatial indicators for at risk locations of developing pvWMHs in the future. To that end, we spatially correlate both fields with pvWMH thickness measured along the ventricular wall to confirm our hypothesis. Additionally, we explore the role of the septum pellucidum, a thin vertical membrane that divides the ventricle's main body into left and right chambers, on the mechanical loading of the ventricular wall to provide a mechanics-based rationale for its presence in the brain. In our models, we apply physiological loading states associated with hemodynamic pulsation to identify wall sections associated with maximum ependymal cell loading and their spatial overlap with pvWMH locations. We ultimately aim to show that the distribution of mechanical loads along the ventricular wall is a good spatial indicator for the risk of developing pvWMHs with advanced age.

2. Methods

2.1. Subject selection and model generation

We adapted previously created finite element models of eight healthy, cognitively normal subjects from the New York University Alzheimer's Disease Research Center (Visser et al., 2021). We only considered cognitively normal subjects without brain pathology such as tumor, neocortical infarction, multiple sclerosis, and diabetes. Subjects were then selected to reflect a broad range of ventricular geometries; specifically, we picked a male and female subject from the 20th, 40th, 60th, and 80th percentile of total intracranial CSF volume (Visser et al., 2021). Subjects provided IRB approved consent for a protocol investigating risk factors of cognitive decline and Alzheimer's disease. Each subject underwent structural MRI on a 3T Siemens Magnetome Prisma (Siemens Healthineers USA). The exam included a high-resolution T1-weighted MPRAGE sequence (TR = 2100 ms, TE = 5 ms, TI = 900 ms, FA = 9°, 256 x 256 x 176 matrix, 1 x 1 x 1 mm voxels, GRAPPA2 acceleration) and a FLAIR sequence used to assess WM lesions (TR = 9000 ms, TE = 75 ms, TI = 2500 ms, FA = 120°, 320 x 196 x 40, 0.7 x 0.7 x 4 mm voxels, GRAPPA2 acceleration). Our subjects had no gross pathology such as tumor, neocortical infarction or hemorrhage. Participants were interviewed according to the Brief Cognitive Rating Scale, rated 1 or 2 on the Global Deterioration Scale (GDS) (Reisberg et al., 1988), and scored at least 27 points on the Mini Mental State Examination (Tombaugh and McIntyre, 1992).

Fig. 2 summarizes the modeling and simulation process described in detail in our previous work (Visser et al., 2021). We select the axial MRI

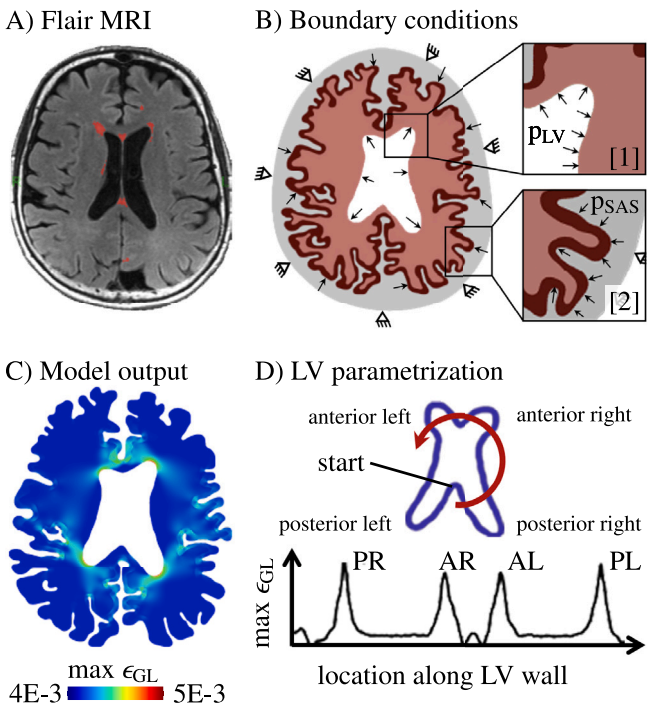

Fig. 2. Model generation process: (A) We select the axial slice with the largest ventricular area and identify the pvWMH (red mask). (B) We segment gray matter, white matter, and cerebrospinal fluid, create a 2D finite element model, and mimic hemodynamic loading by applying a normal pressure to the ventricular surface [B1] and the CSF-gray matter interface [B2]. (C) Representative output of maximum principal Green Lagrange strain. (D) We parametrize the lateral ventricular wall to plot the variation of mechanical output measures along its perimeter.

slice with the largest ventricular surface area (Fig. 2A) as mechanical loads will be highest in this cross-section. We segment the slice into CSF (gray), gray matter (dark red), and white matter (light red) using Simpleware (Synopsis, Mountain View CA) (Fig. 2B). In the present work, we do not segment deep gray matter structures, such as the caudate and thalamus, for the lack of available material properties and model them as white matter. We performed a mesh convergence study to determine an adequate mesh refinement level which balances computational cost and sufficient mesh refinement along the ventricular wall to provide reliable predictions of wall loading, see our supplementary materials for details. The individual brain segmentations are ultimately converted into FE meshes with a minimum and maximum edge length of 0.5 mm and 1.0 mm, respectively. We import our meshes into Abaqus (Dassault Systemes, Vélizy-Villacoublay, France) where we apply our desired boundary conditions. Given the pulsatile motion of the brain, tissues undergo cyclic deformations. To approximate maximum ventricular loading from hemodynamic pulsation, we limit our analysis to a plane-strain, quasi-static analysis at peak fluid pressure and prescribe a normal pressure on the ventricular surface of magnitude $p_{LV} = 0.15$ mmHg (Zhu et al., 2006; Butler et al., 2017), and a normal pressure on the gray matter-CSF interface of magnitude $p_{SAS} = 0.0075$ mmHg. Fluid pressure fluctuates around a "mean pressure level" ranging from 5–15 mmHg (Raboel et al., 2012). We assume here, that the brain is in its undeformed state at this mean pressure level and therefore prescribe the maximum pressure difference as the best approximation of the loading state. The ventricle to gray matter surface pressure ratio is based on experiments showing that SAS pressure is only 10%–20% of the ventricular pressure (Linninger et al., 2005; Zhong et al., 2009). We model the skull by pinning the nodes on the outer CSF boundary. Simulation results are reported as fields (Fig. 2C) or evaluated along the lateral ventricular wall (Fig. 2D). We parametrize the ventricular wall starting at the posterior edge of the LV's main body and move counterclockwise. This allows us to analyze mechanomarker level variations along the ventricular wall and to spatially correlate ependymal cell loading with pvWMH locations.

It has been shown that the mechanical response of brain tissue is best captured by a one-term Ogden model given by the strain energy density function, Ψ, (Weickenmeier et al., 2016; Visser et al., 2021)

$$\Psi = \frac{\mu}{2}[\bar{\lambda}_1^2 + \bar{\lambda}_2^2 + \bar{\lambda}_3^2 - 3] + \frac{\kappa}{4}[J^2 - 1 - 2\log(J)], \tag{1}$$

with shear modulus μ governing distortional deformation and bulk modulus κ governing dilatational deformation. J is the Jacobian of the deformation gradient $\mathbf{F}$ which is the spatial mapping from the reference to the current configuration and $\bar{\lambda}_1$, $\bar{\lambda}_2$, and $\bar{\lambda}_3$ are the isochoric principal stretches. A detailed derivation of the basic continuum equations is available here (Visser et al., 2021). We assume our material to be nearly incompressible with a Poisson's ratio of 0.45 and a white-gray matter stiffness ratio of 2 (Weickenmeier et al., 2016). Specifically, we chose experimentally-informed constants $\mu = 0.34$ kPa and $\kappa = 3.3$ kPa for gray matter and $\mu = 0.68$ kPa and $\kappa = 6.6$ kPa for white matter (Linninger et al., 2005; Weickenmeier et al., 2016; van Dommelen et al., 2010; Kaster et al., 2011; Budday et al., 2015). We approximate CSF as an ultrasoft, compressible material with a Young's modulus of 0.1 kPa and a Poisson's ratio of 0.3. This modeling approach provides a suspension of the brain inside the skull while creating minimal resistance to brain deformations from loading (Blinkouskaya et al., 2021). The Ogden model was implemented as a user material subroutine (UMAT) following the example of Connolly et al. (2019). We investigate the impact of the septum pellucidum, by creating a second model for each subject where we mimic the mechanical function of the septum pellucidum by adding three linear spring elements which connect the anterior and posterior edges of the ventricle's main body, see Fig. 6. We prescribe a linear spring stiffness of 1 N/mm based on two considerations: (1) to the best of our knowledge, there is no experimental data on the mechanical properties of the septum pellucidum in literature; (2) the selected spring stiffness is high enough to constrain the spring's elongation under the prescribed loading case. This creates the other extreme case in comparison to simulations without any septum.

2.2. Mechanomarkers of ependymal cell loading

In addition to ventricular horn radius introduced in previous work (Visser et al., 2021), we propose additional mechanomarkers to substantiate our proposed periventricular white matter damage mechanism. We pose that curvature of the ventricular wall and ependymal cell stretch are good indicators for long-term pvWMH locations. To that end, we spatially correlate both fields with pvWMH thickness measured along the ventricular wall to confirm our hypothesis.

Measures of cellular stretch are based on cellular deformations along the ventricular wall. We differentiate between cell stretch in the direction tangential to the ventricular wall λ_t and ependymal cell stretch in the direction normal to the ventricular wall λ_n. Cell stretches λ_t and λ_n are given by

$$\lambda_t = \sqrt{\mathbf{t} \cdot \mathbf{C}\,\mathbf{t}} \quad \text{and} \quad \lambda_n = \sqrt{\mathbf{n} \cdot \mathbf{C}\,\mathbf{n}}, \tag{2}$$

where $\mathbf{C}$ is the right Cauchy–Green deformation tensor and $\{\mathbf{t}, \mathbf{n}\}$ are the unit vector tangential and normal to the ventricular wall. Unit vectors are updated after each converged increment of the finite element simulation. From cell stretch and compression, we also compute a thinning ratio $\tau = \lambda_t/\lambda_n$. These measures characterize the ependymal cell thinning observed in pathology (Granados-Durán et al., 2016). We determine the initial normal ($\mathbf{n}_0$) and tangential ($\mathbf{t}_0$) wall directions from a Laplacian diffusion simulation for each of our eight FE models, see Visser et al. (2021).

We assess local curvature as an additional marker for possible pvWMH locations. Mechanically, regions with high curvature are inherently prone to increased stretch. Based on the discrete representation

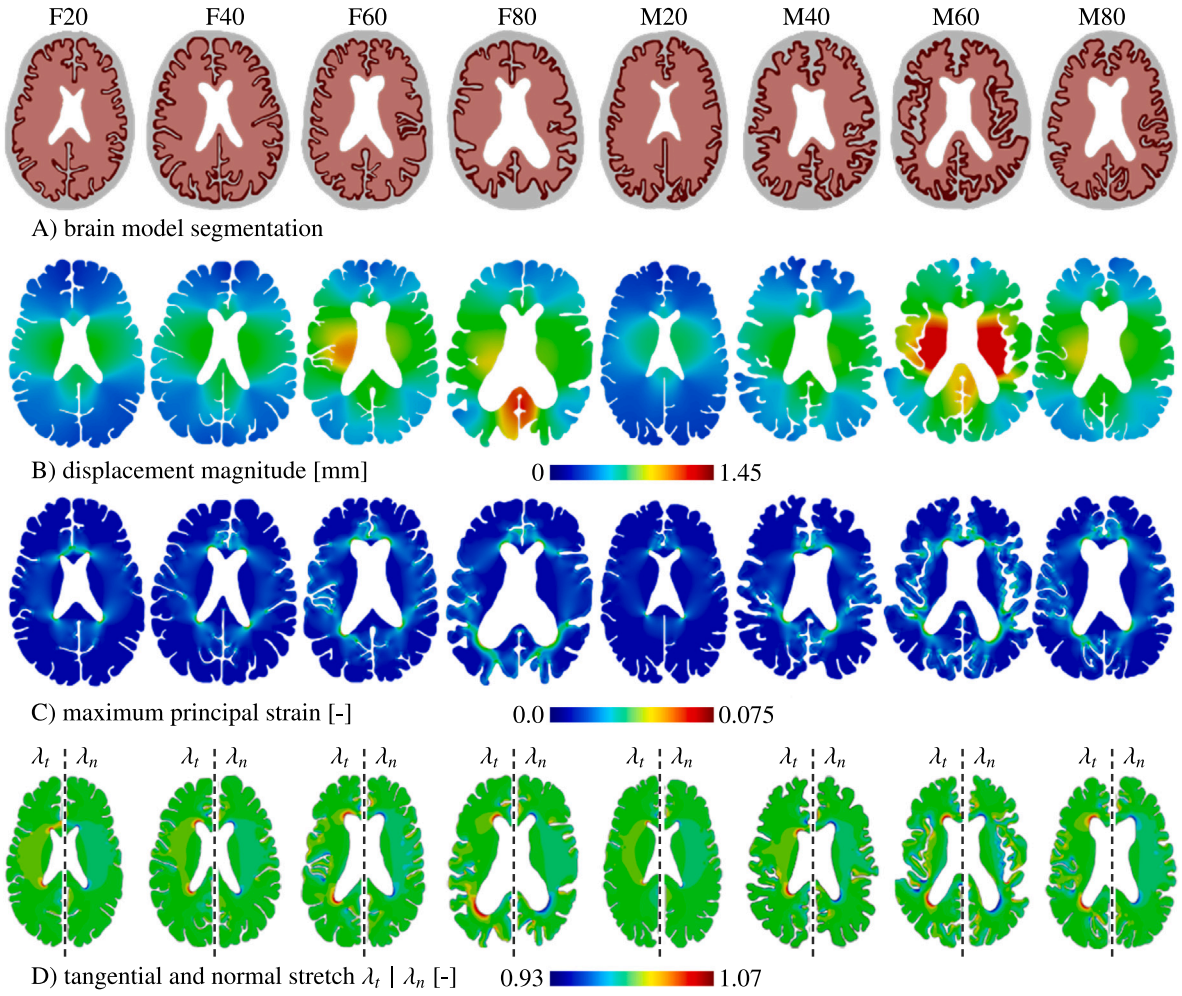

Fig. 3. Simulation results for all eight models during peak loading: (A) brain tissue segmentations converted into FE models; (B) displacement magnitude at peak hemodynamic loading [mm]; (C) maximum principal strain [-]; (D) left hemispheres show the tangential stretch field and the right hemispheres show the normal stretch fields [-]. Tangential and normal stretch fields are similar with respect to left and right hemisphere.

of the ventricular wall by a set of nodes, we calculate Menger curvature as the reciprocal of radius R of the circle that passes through the three proximal points on the wall. To reduce sensitivity to positional error inherent in 1 mm spatial resolution of segmented MRI, curvature is calculated based on a subset of every 10th node. Curvature K is given by

$$K(n_1, n_2, n_3) = \frac{4\,A}{|n_1 - n_2||n_2 - n_3||n_3 - n_1|}, \tag{3}$$

where A denotes the area of the triangle spanned by n_1, n_2, n_3 and $|n_i - n_j|$ denotes the Euclidean distance between points n_i and n_j.

From each subject's pvWMH masks we calculate a local measure of WMH thickness. First, we use a custom-code to co-register our eight 2D FE meshes with their corresponding axial FLAIR image. Our algorithm maximizes the overlap of the outer gray matter and lateral ventricular contours of the FE model and respective tissue segmentations of the axial slice. Next, we calculate the centroid of each element in our meshes and interpolate their coordinates in the respective image space to determine which elements coincide with pvWMH locations. In a final step, for each node along the ventricular wall, we check if it belongs to an element that coincides with a pvWMH location; if it does, we use the unit vector normal to the ventricular wall to determine all additional pvWMH-elements that intersect with this vector's direction. Local pvWMH thickness is defined as the distance from the node on the ventricular wall to the furthest pvWMH.

2.3. Statistical analysis

Statistical analysis was performed using Matlab. Results are reported as mean ± standard deviation (SD). To analyze the statistical significance of differences between regions with or without pWMHs, each LV wall was resampled into 1500 equidistant points. These points were divided by the presence or absence of pWMH, yielding a total of 7423 points without pWMH and 4577 points with pWMH. Subsequently, a Two Sample T-test was performed. Correlation between two parameters of interest was measured by the Pearson correlation coefficient. Both test statistics were reported with test statistic t, degrees of freedom, and p value.

3. Results

3.1. Mechanical loading of periventricular tissues from ventricular expansion

Fig. 3 shows simulation results at peak hemodynamic loading. The first row shows each subject's CSF, gray matter, and white matter segmentation used to create our finite element models. The second row shows the displacement magnitude field with values up to 1.45 mm which agrees with previously reported wall displacements (Abderezaei et al., 2020; Soellinger et al., 2009). We observe a consistent deformation patterns across all our models: the lateral ventricle's main body deforms most; the anterior and posterior parts of the brain displace

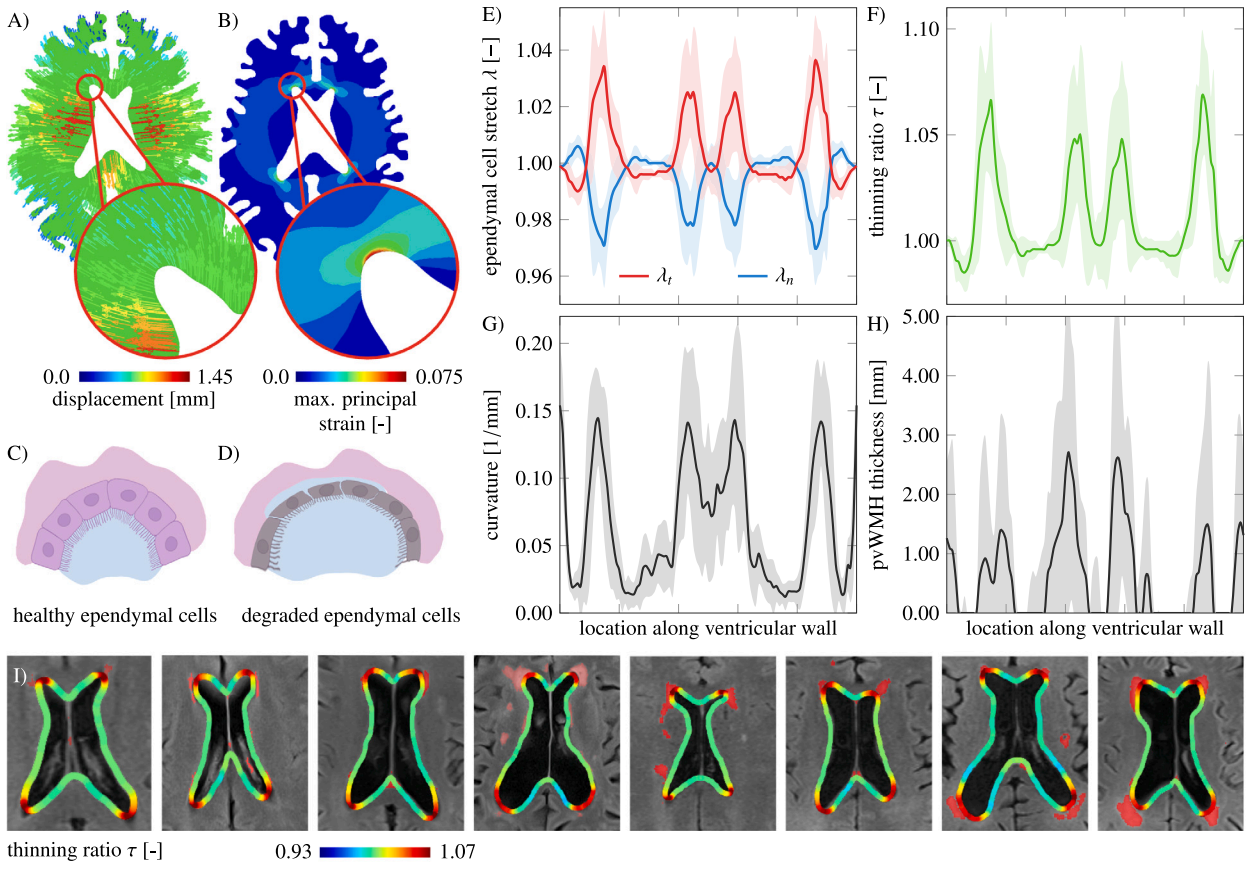

Fig. 4. Representation of the brain's (A) local displacement magnitudes and corresponding displacement vectors and (B) maximum principal strain field. Schematic representation of our proposed damage mechanisms that shows the (C) healthy ependymal wall and (D) degraded ependymal lining which causes CSF leakage into periventricular tissues. Mean mechanomarker distribution along the parameterized ventricular wall based on results from all 8 models: (E) tangential stretch λ_t in red and normal stretch λ_n in blue; (F) thinning ratio, (G) curvature of the LV wall; and (H) pvWMH thickness measured from MRI. The figures in bottom row (I) show the superposition of the WMH mask from FLAIR and the thinning ratio. We observe a consistent spatial overlap between pvWMH location and elevated ependymal cell thinning.

much less with the exception of model F80 for which there is less brain matter in the posterior part of the brain in comparison to all other models. From an ependymal cell perspective, large displacements do not strictly mean high cellular loading. For example, a uniform local displacement field, such as predominantly observed for the lateral ventricle's main body, leads to low strain. High relative displacements, however, lead to increased cellular distortions. In the third row, we show the maximum principal strain field which is a more suitable property to assess the severity of cellular deformations. We observe that the anterior and posterior horns are particularly affected by such elevated local strains due to their "ballooning" effect, that is their radial expansion with hemodynamic loading. For all subjects, the maximum principal strain field shows peak levels in the lateral ventricle's anterior and posterior horns which gradually decrease when moving away from the ventricular wall. Maximum values of up to 8% are very localized in the tips of the horns which demonstrates their particular vulnerability to mechanical damage over time. Strikingly, the maximum principal strain field is fairly independent of lateral ventricular shape and size which is an indicator for the consistency of mechanical loads on ependymal cells across the population. The fourth row show the tangential stretch (left hemisphere) and the normal stretch (right hemisphere) fields with values ranging from −7% to +7% stretch. Similar to the maximum principal strain field, peak values consistently appear in the anterior and posterior horns and decrease radially when moving away from the wall. The lateral ventricle's main body experiences nearly no ependymal cell stretch. Moreover, it is evident that increased stretch levels extend to periventricular white matter tissue near the horns as well. Given the spatial overlap with typical pvWMH locations, this suggests a significant mechanics-driven interplay between ependymal cell loading, white matter tissue compression, hypoperfusion, and tissue damage due to ventricular expansion.

3.2. Ependymal cell loading along the ventricular wall

Fig. 4 outlines the mechanical loading state of ependymal cells along the ventricular wall. Fig. 4(A) shows a representative image the displacement vector field of model F20 with a magnification of the left anterior horn. The radial distribution of displacement vector in the horn is indicative of large cellular distortions which is reflected in the local concentrations of strain shown in Fig. 4(B). This loading state causes healthy wall anatomy shown in Fig. 4(C) to gradually degenerate into a degraded wall with ependymal cells that are stretched thin and intercellular junctions that erode causing CSF influx into periventricular tissues. We parametrize the ventricular wall to quantify the variation of our other mechanomarkers along the wall. Our parametrization begins at the posterior edge of the ventricle's main body and continues counterclockwise (see Fig. 2D). Fig. 4(E) shows the mean and SD of the tangential stretch (red) and normal stretch (blue) along the wall and clearly reveals four peaks that coincide with the anterior and posterior horns (first peak belongs to the right posterior, the second peak to the right anterior, the third peak to the left anterior, and the fourth peak to the left posterior horn, respectively). Average maximum tangential stretch λ_t is 1.061 ± 0.01 (1.062 ± 0.009 for females and 1.059 ± 0.011 for males). Average minimal normal stretch λ_n is 0.951 ± 0.007 (0.95 ± 0.006 for females and 0.952 ± 0.007 for males). From tangential and normal stretch we calculated a thinning

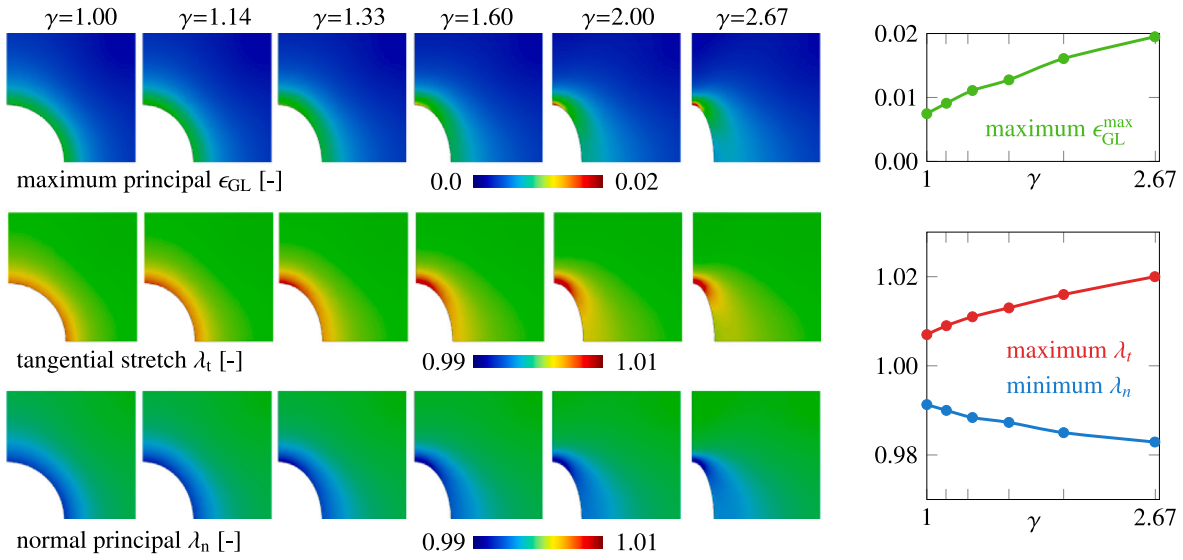

Fig. 5. Surrogate models of ventricular horns with varying curvature measured by γ, i.e., the ratio of the ellipsoid's long and short axis. We report the maximum principal Green Lagrange strain (top row), tangential stretch field λ_t (middle row), and normal stretch field λ_n (bottom row) of the ventricular wall. The top right graph shows peak maximum Green Lagrange strain for increasing γ and the bottom right graph shows maximum tangential and minimum normal stretch for increasing γ.

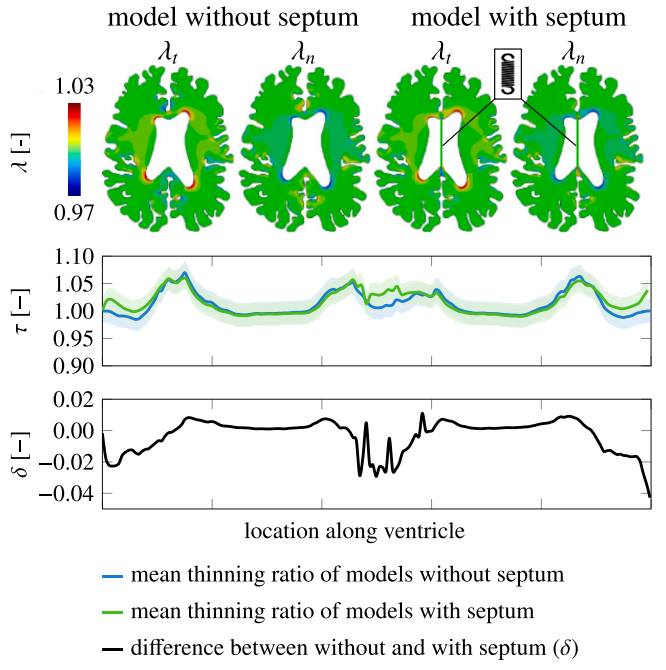

Fig. 6. Impact of the septum. The first row shows the tangential λ_t and normal λ_n stretch fields for model M40 without the septum (left two images) and with the septum (right two images). Second row, mean and standard deviation of the thinning ratio for models without the septum (blue) and with the septum (green). Third row, shows the difference between the thinning ratio without the septum (default) and with the septum.

ratio which indicates the degree of cellular thinning resulting from ventricular wall expansion. Fig. 4(F) shows the mean and SD of the thinning ratio which follows the same pattern. Average maximum thinning ratio is 1.12 ± 0.018 (1.12 ± 0.017 for females and 1.11 ± 0.019 for males). Large sections of the ventricular wall experience almost no ependymal cell thinning ($\tau \approx 1$), while wall sections with thinning ratio τ above 1 are limited to the horns. We observe very good spatial overlap between thinning ratio and pvWMH location, as indicated by Wilcoxon rank sum test with z=−6.3, p<.001%. We show a direct comparison between mechanomarkers, i.e., stretch, thinning ratio, and curvature, in locations with and without pvWMHs in Fig. S2 in the supplementary materials. Based on an effort to identify a thinning ratio threshold for which wall sections are likely also affected by pvWMHs thickness larger than 0 summarized in Fig. S3 in the supplementary materials, we find that a thinning ratio above 1.043 is a reliable marker to predict pvWMH locations. Fig. 4(G) shows curvature of the ventricular wall. Despite significant variations in ventricular shape, the horns have highest curvature which consistently overlaps with high cellular loading. Maximum average curvature is 0.066 ± 0.06 1/mm (0.068 ± 0.06 1/mm in females and 0.063 ± 0.059 1/mm in males). In comparison to stretch-related measures, curvature is also high in the anterior and posterior edges of the ventricle's main body. Furthermore, curvature is significantly higher at nodes with pvWMHs (thickness > 0) in comparison to nodes without pvWMHs based on a Wilcoxon rank sum test with z=−6.2, p < 0.001%. Based on the same threshold identification approach mentioned for the thinning ratio above, we observe that a curvature threshold of 0.128 is a good predictor for pvWMH locations, see Fig. S3. From comparison of individual model results, we observe that more rounded horns, i.e., in models F80 and M60 for example, exhibit smoother thinning ratio peaks, while sharp horns, i.e., in models M20 and F20 for example, have more pronounced peaks of ependymal thinning. Fig. 4(H) shows pvWMH thickness with an average maximum thickness of 7.4 ± 1.49 mm (6.5 ± 1.3 mm for females and 8.4 ± 1.66 mm for males). PVWMH thickness exhibits significantly more variation across all subjects due to variations with respect to their disease state and age. Overall, we observe that our mechanomarkers based on stretch and curvature show statistically significant spatial overlap with pvWMH thickness. This is further supported by Fig. 4(I) where we overlay thinning ratio magnitude with the pvWMH masks generated from FLAIR imaging for all eight subjects. Bright red wall sections with maximum cell thinning ratio overlap show very good agreement with pvWMH locations.

3.3. Horn geometry affects ependymal cell loading

Fig. 5 shows our surrogate model to analyze the effect of horn curvature on ependymal cell loading. We approximated the ventricular horn by an ellipsoid and created six instances with an aspect ratio γ, i.e. the ratio of their major axis to their minor axis, ranging from 1 (which is equivalent to a circle) to 2.67 (representative of a sharp horn).

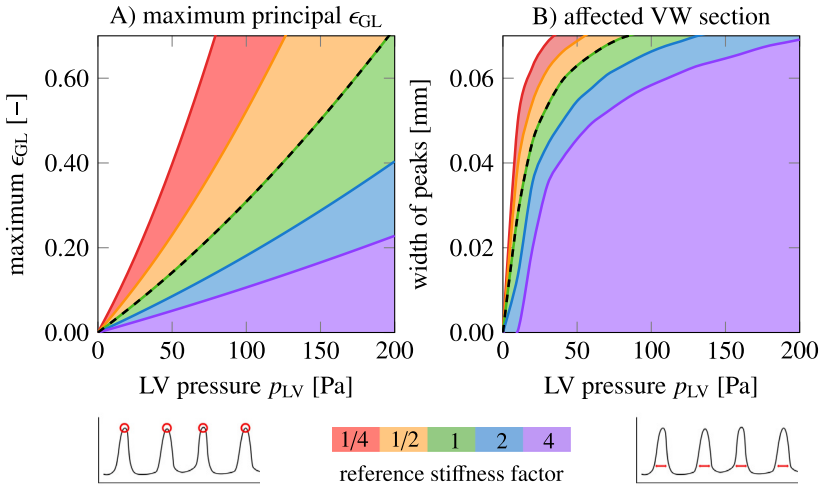

Fig. 7. Model sensitivity to stiffness and pressure. (A) An increase in pressure or a decrease in stiffness leads to increased peak Green Lagrange strains. (B) An increase in pressure or decrease in stiffness also increases the ventricular wall (VW) section affected by strains > 0.01.

We prescribe the same material behavior and loading conditions per our brain models. For increasing γ, strain and stretch fields become increasingly heterogeneous with a clear concentration of peak values in the tip of the horn. For sharper horns, the edge of the ventricle experiences high tangential stretch and pronounced compression in normal direction. This is consistent with our brain model results and highlights the viability of horn geometry as a biomarker for pvWMH formation.

3.4. Impact of the septum pellucidum on ependymal cell loading

Fig. 6 shows the impact of the septum pellucidum on the distribution of tangential and normal stretches in our model as well its effect on the thinning ratio. We observe that the tangential and normal stretch fields are nearly identical for the entire axial slice except for the immediate vicinity of the spring attachment points which mimic the insertion points of the septum into parenchyma. The thinning ratio (second row) overlaps for large sections of the ventricular wall but differs at the septum's anterior and posterior anchoring points. Comparison of models without and with the septum suggests that the septum locally increases the thinning ratio in exactly the locations that WMHs are often observed. Although the thinning ratio stays below the threshold reported in Section 3.2, it accurately indicates that these additional wall sections are subject to damage and at risk for pvWMH formation.

3.5. Model sensitivities to tissue stiffness and ventricular pressure

Fig. 7 shows the effect of tissue stiffness and ventricular pressure on maximum principal Green Lagrange strain and area of the ventricular wall exposed to increased strains. Tissue stiffness varies from subject to subject and is severely affected by aging (Blinkouskaya et al., 2021; Brown et al., 2005). Neurodegenerative processes associated with metabolic slowing, wear, and homeostatic dysregulation leads to progressive tissue softening. Age-related cardiovascular changes are linked to increased hemodynamic loads, cerebral small vessel disease, and an increase in fluid pressure in the skull (Blinkouskaya et al., 2021). Our previous paper showed that the pattern of mechanical loading along the LV remains quite similar independent of brain tissue stiffness and LV pressure changes (Visser et al., 2021). The current sensitivity analysis suggests that periventricular tissues are more affected by changes in LV pressure than changes in stiffness. This plays a major role in identifying suitable intervention strategies. It appears crucial to manage hemodynamic pressure and maintain good cardiovascular health in order to minimize ependymal cells degeneration along the ventricular wall.

4. Discussion

The present work provides a mechanistic mechanism to rationalize the onset locations of pvWMHs. We created eight subject specific models with a broad range of ventricular volumes and demonstrate through computational modeling that ventricular wall sections with peak ependymal cell loading coincide with pvWMH locations. In the following we discuss our proposed mechanism in light of the current understanding of pvWMH etiology and elaborate on the role of ventricular geometry and the septum on pvWMH formation.

4.1. Does ependymal cell damage lead to pvWMH formation?

Ventricular expansion due to cerebral atrophy and pulsatile ventricular expansion due to hemodynamic loading cause the ventricular wall to stretch (Blinkouskaya et al., 2021; Visser et al., 2021). Equivalent to a balloon expanding upon inflation, the ventricular wall expands and causes the cells lining the wall to be stretched thin. The load is carried by the cells which are stretched thin as well as the tight cadherin junctions responsible for maintaining cellular connectivity (Oliver et al., 2013; Veeraval et al., 2020). The continuous expansion of the ventricles during aging gradually stresses the wall. The overlying cyclic loading with every heartbeat further challenges the cadherin junctions to maintain local homeostasis and directed fluid exchange at the interface between CSF and parenchyma. Over time, degeneration of the ependymal cell layer (Sarnat, 1995) causes unregulated influx of CSF into periventricular white matter (Jiménez et al., 2014). Subsequent edema, inflammation, and other secondary damage mechanisms degrade axons, cause astrogliosis (Luo et al., 2008), and contribute to parallel damage mechanisms associated with cerebral small vessel disease. The resulting cascade is thought to be irrecoverable and leads to the progressive growth of white matter lesions into deeper white matter structures. This study shows that mechanically, the ventricular wall is inherently loaded most where curvature is high. This applies to the ventricular horns and the edges of the ventricle's main body, see Fig. 4(I). Statistical analysis in the current study is limited by a low sample size of 8 models. From a mechanics perspective, however,

the similarity of lateral ventricular shapes across all human brains is sufficient to demonstrate the consistent localization of peak mechanical loading in ventricular horns. Future work should incorporate a larger sample of subjects with similar ventricular and pvWMH properties.

Pathophysiologically, it has been shown that local junction protein degeneration along the ventricular wall drives ependymal cell denudation with subsequent astroglial scaring (Roales-Buján et al., 2012). These locations were identified to be along the edge of the ventricles main body and ventricular horns (Scheltens et al., 1995). Denudation typically starts with the detachment of few ependymal cells before denudation radially expands from these initiation sites (Oliver et al., 2013). Disruption of the ventricular wall triggers subependymal astrocytes to cover denuded wall sections. Resulting astroglial scars are able to restore ependymal-like features although controlled fluid exchange is permanently disrupted. We pose that ependymal cell denudation is caused by junction protein degeneration from mechanical fatigue in the aging brain. Sarnat et al. reported ependymal cell thinning, loss of apical-basal polarization, and ventricular scaring in older subjects and patients with increased ventricular pressure (Sarnat, 1995). Mechanically, as the ependymal cellular lining thins out with aging, internal stresses resulting from ventricular wall deformation will increase causing an additional burden on intercellular junctions and preservation of the wall's fluid barrier function. The pervasive presence of WMHs in nearly every brain is a strong indicator that mechanical loading is a critical contributor to its onset. The good spatial overlap between the proposed mechanomarker *thinning ratio* is a suitable measure to identify locations along the ventricular wall that are at risk of developing pvWMHs in the future. Given the extensive shape changes during aging, a longitudinal model is required to determine a suitable threshold level that reliably differentiates between pvWMH location or healthy ventricular wall irrespective of a subject's brain shape, age, or tissue properties.

4.2. How do lateral ventricle shape and the septum affect pvWMH locations?

The shape of the lateral ventricles plays a critical role in the magnitude of mechanical loading on the ventricular wall (Visser et al., 2021). The locally varying neuroanatomy of periventricular tissues determines the wall's ability to sustain these gradually increasing strains resulting from cerebral atrophy and hemodynamic loading. We verified that our predicted wall deformations agree with in vivo measurements performed using phase-based amplified MRI (Holdsworth et al., 2016; Terem et al., 2018). Mechanically, high curvature, or small horns, are associated with high tangential and normal stretch. Therefore, younger brains with little cerebral atrophy experience higher loads in comparison to brains with ventricular enlargement resulting in larger horns. This observation is significant evidence for a mechanics-based damage mechanisms behind pvWMH formation, as younger brains are characterized by smaller ventricles and sharper horns in comparison to older brains. Ventricular enlargement is generally not only linked to an overall increase in volume but also an increase in horn size (Todd et al., 2018). Hemodynamic loading imposes additional loads included in the present work which demonstrates that peak loading persists in the horns irrespective of ventricular volume. A potential marker to predict pvWMH formation could be the rate at which curvature changes with age. Higher rates would indicate accelerated atrophy and, therefore, increased ventricular wall loading.

Our simulations show that the septum pellucidum does not impact the magnitude and location of maximum tangential and normal stretch along the ventricular wall. We observe, however, that the septum leads to an elevated thinning ratio in the anterior and posterior anchoring points of the septum with white matter. This spatial overlap may very well explain why white matter hyperintensities are frequently found in these locations as well. Abnormalities, or even the absence, of the septum pellucidum are linked to several neurological conditions; yet, the septum's role, if any, remains poorly understood (Khanra et al., 2016). Considering ventricular enlargement resulting from cerebral atrophy during aging, for example, the septum might actually mitigate increased ventricular wall loading by constraining radial expansion and preserve the mechanical integrity of the fluid-brain barrier. In the present work, we approximate the septum as a nearly rigid material to explore the two extreme cases: unconstrained ventricular expansion (no septum in the model) and the constrained case with no extension between the septum's anchoring points (septum included). To the best of our knowledge, the septum's mechanical properties have never been reported in literature before, such that corresponding mechanical tests would provide insight into age-related stiffness changes of this particular tissue. Key questions worth investigating include: Does the septum stretch out over time? Does the septum disintegrate due to cell damage (Gardner et al., 2016; Acabchuk et al., 2016)? How does the septum influence ventricular expansion from cerebral atrophy?

4.3. Limitations

This study is not without limitations. Our analysis is based on 2D models and therefore disregards the more complex three dimensional deformation behavior of the expanding ventricles. Future work, should aim reconstructing the entire brain and evaluation the spatial distribution of ependymal cell stretches across the entire ventricular wall. Most likely, areas with elevated curvature such as the ventricular horns as well as the anterior and posterior edge of the ventricle's main body, will exhibit increased mechanical loading. It needs to be verified how well our proposed mechanomarkers coincide with those pvWMH locations. Moreover, we recognize that the ventricular wall is a multilayered structure which we approximate as white matter instead of differentiating between ventricular wall layers I-III. Future work needs to address this concern in order to derive a better prediction of ependymal cell-level strains and stretches to ultimately improve our spatial predictions of possible pvWMH formation. Secondly, the proposed model assumes hemodynamic loading to drive ventricular wall expansion. While this choice of loading condition captures the pulsatile loading state of the ventricular wall, it does not account for long-term ventricular expansion caused by cerebral atrophy (Blinkouskaya et al., 2021). Ventricular expansion will have a significant impact on ependymal cell loading since ventricles typically increase by several hundred percent as a result of natural aging. Lastly, our current model does not provide a prediction for pvWMH growth. This preliminary work demonstrates where pvWMHs are most likely to appear first. Future work should provide a modified model that captures the progressive changes of the underlying tissue damage along the ventricular wall. Mechanics-driven ependymal over-loading leads to CSF leakage into periventricular tissues and secondary damage mechanisms which results in pvWMH changes and their gradual penetration into deep white matter tissue (Schmidt et al., 2005; Sachdev et al., 2007). This model should be validated against longitudinal FLAIR image data that allows to quantify progressive pvWMH growth.

5. Conclusion

The strain state of the ventricular wall causes ependymal cells to be stretched thin, thus creating increased loads on ependymal cells and their connecting intercellular junctions. Our modeling approach suggests that ventricular geometry dictates pvWMH location and that mechanics likely plays a central role in degrading ependymal cell integrity, thus leading to unregulated fluid exchange between ventricles and parenchyma. We also conclude that including the septum in our models introduces additional ventricular wall section exposed to increased mechanical loading by constraining the extent of ventricular expansion during aging. We therefore submit that brain shape and mechanical loading states are both reliable indicators for at risk ventricular wall sections. Our proposed mechanisms must not be understood

to be in conflict with the existing notion that pvWMHs are of vascular origin, but that we have to understand WMH etiology as a more complex interplay between vascular degeneration and ventricular wall failure.

Funding

This work was supported by the National Institute of Biomedical Imaging and Bioengineering of the National Institutes of Health, United States under award U24EB028980 to Henry Rusinek for developing the FireVoxel software and the National Institute on Aging of the National Institutes of Health, United States under award R21AG067442 to Johannes Weickenmeier. MRI and clinical data were obtained from the Alzheimer's Disease Research Center supported by the National Institute on Aging of the National Institutes of Health, United States under award P30AG066512.

CRediT authorship contribution statement

Valery L. Visser: Writing – original draft, Visualization, Software, Methodology, Formal analysis, Data curation, Conceptualization. **Andreia Caçoilo:** Writing – review & editing, Writing – original draft Methodology, Investigation, Data curation. **Henry Rusinek:** Writing – review & editing, Writing – original draft, Supervision, Funding acquisition, Conceptualization. **Johannes Weickenmeier:** Writing – review & editing, Writing – original draft, Visualization, Supervision, Project administration, Methodology, Investigation, Funding acquisition, Formal analysis, Data curation, Conceptualization.

Declaration of competing interest

The authors declare the following financial interests/personal relationships which may be considered as potential competing interests: Johannes Weickenmeier reports financial support was provided by National Institutes of Health. Henry Rusinek reports financial support was provided by National Institutes of Health.

Data availability

Data will be made available on request.

Appendix A. Supplementary data

Supplementary material related to this article can be found online at https://doi.org/10.1016/j.jmbbm.2023.105921.

References

Abderezaei, J., Martinez, J., Terem, I., Fabris, G., Pionteck, A., Yang, Y., Holdsworth, S.J., Nael, K., Kurt, M., 2020. Amplified flow imaging (aflow): A novel mri-based tool to unravel the coupled dynamics between the human brain and cerebrovasculature. IEEE Trans. Med. Imaging 39.

Acabchuk, R., Briggs, D.I., Angoa-Pérez, M., Powers, M., Wolferz Jr., R., Soloway, M., Stern, M., Talbot, L.R., Kuhn, D.M., Conover, J.C., 2016. Repeated mild traumatic brain injury causes focal response in lateral septum and hippocampus. Concussion 1, CNC13.

Al-Anbari, H.S.N., Ismail, D.K., Hasan, M.K., Aga, Q.A.A.K., Shinu, P., Nair, A.B., 2020. High blood lead levels: An increased risk for development of brain hyperintensities among type 2 diabetes mellitus patients. Biol. Trace Elem. Res. 4, 1–9.

Armstrong, N.J., Mather, K.A., Sargurupremraj, M., Knol, M.J., Malik, R., Satizabal, C.L., Yanek, L.R., Wen, W., Gudnason, V.G., Dueker, N.D., et al., 2020. Common genetic variation indicates separate causes for periventricular and deep white matter hyperintensities. Stroke 51, 2111–2121.

Blinkouskaya, Y., Caçoilo, A., Gollamudi, T., Jalalian, S., Weickenmeier, J., 2021. Brain aging mechanisms with mechanical manifestations. Mech. Ageing Dev. 200, 111575.

Blinkouskaya, Y., Weickenmeier, J., 2021. Brain shape changes associated with cerebral atrophy in healthy aging and alzheimer's disease. Front. Mech. Eng. 64.

Brown, R.C., Lockwood, A.H., Sonawane, B.R., 2005. Neurodegenerative diseases: An overview of environmental risk factors. Environ. Health Perspect. 113, 1250–1256.

Bruni, J.E., Del Bigio, M., Clattenburg, R., 1985. Ependyma: normal and pathological. a review of the literature. Brain Res. Rev. 9, 1–19.

Budday, S., Nay, R., de Rooij, R., Steinmann, P., Wyrobek, T., Ovaert, T.C., Kuhl, E., 2015. Mechanical properties of gray and white matter brain tissue by indentation. J. Mech. Behav. Biomed. Mater. 46, 318–330.

Butler, W.E., Agarwalla, P.K., Codd, P., 2017. CSF in the ventricles of the brain behaves as a relay medium for arteriovenous pulse wave phase coupling. PLoS ONE 12.

Caçoilo, A., Rusinek, H., Weickenmeier, J., 2022. 3D finite-element brain modeling of lateral ventricular wall loading to rationalize periventricular white matter hyperintensity locations. Eng. Comput. 1–17.

Cheng, C.Y., Cheng, H.M., Chen, S.P., Chung, C.P., Lin, Y.Y., Hu, H.H., Chen, C.H., Wang, S.J., 2018. White matter hyperintensities in migraine: Clinical significance and central pulsatile hemodynamic correlates. Cephalalgia 38, 1225–1236.

Connolly, S.J., Mackenzie, D., Gorash, Y., 2019. Isotropic hyperelasticity in principal stretches: explicit elasticity tensors and numerical implementation. Comput. Mech. 64, 1273–1288.

De Groot, M., Verhaaren, B.F., De Boer, R., Klein, S., Hofman, A., van der Lugt, A., Ikram, M.A., Niessen, W.J., Vernooij, M.W., 2013. Changes in normal-appearing white matter precede development of white matter lesions. Stroke 44, 1037–1042.

Debette, S., Markus, H., 2010. The clinical importance of white matter hyperintensities on brain magnetic resonance imaging: systematic review and meta-analysis. Bmj 341.

Del Bigio, M.R., 2009. Ependymal cells: biology and pathology. Acta Neuropathol. 119 (1), 55–73.

Fazekas, F., Chawluk, J.B., Alavi, A., Hurtig, H.I., Zimmerman, R.A., 1987. Mr signal abnormalities at 1.5 t in alzheimer's dementia and normal aging. Am. J. Roentgenol. 149, 351–356.

Fazekas, F., Kleinert, R., Offenbacher, H., 1993. Pathologic correlates of incidental mri white matter signal hyperintensities. Neurology 43, 1683.

Fazekas, F., Wardlaw, J.M., 2013. The origin of white matter lesions: a further piece to the puzzle.

Fernando, M.S., Simpson, J.E., Matthews, F., Brayne, C., Lewis, C.E., Barber, R., Kalaria, R.N., Forster, G., Esteves, F., Wharton, S.B., Shaw, P.J., O'Brien, J.T., Ince, P.G., 2006. White matter lesions in an unselected cohort of the elderly. Stroke 37, 1391–1398.

Fukuda, H., Kitani, M., 1996. Cigarette smoking is correlated with the periventricular hyperintensity grade on brain magnetic resonance imaging. Stroke 27, 645–649.

Gardner, R.C., Hess, C.P., Brus-Ramer, M., Possin, K.L., Cohn-Sheehy, B.I., Kramer, J.H., Berger, M.S., Yaffe, K., Miller, B., Rabinovici, G.D., 2016. Cavum septum pellucidum in retired american pro-football players. J. Neurotrauma 33, 157–161.

Gouw, A.A., Van Der Flier, W.M., Fazekas, F., Van Straaten, E.C.W., Pantoni, L., Poggesi, A., Inzitari, D., Erkinjuntti, T., Wahlund, L.O., Waldemar, G., Schmidt, R., Scheltens, P., Barkhof, F., 2008. Progression of white matter hyperintensities and incidence of new lacunes over a 3-year period the leukoaraiosis and disability study. Stroke 39, 1414–1420.

Granados-Durán, P., López-Ávalos, M.D., Hughes, T.R., Johnson, K., Morgan, B.P., Tamburini, P.P., Fernández-Llebrez, P., Grondona, J.M., 2016. Complement system activation contributes to the ependymal damage induced by microbial neuraminidase. J. Neuroinflammation 13, 1–15.

Holdsworth, S.J., Rahimi, M.S., Ni, W.W., Zaharchuk, G., Moseley, M.E., 2016. Amplified magnetic resonance imaging (amri). Magn. Reson. Med. 75, 2245–2254.

Jiménez, A.J., Domínguez-Pinos, M.D., Guerra, M.M., Fernández-Llebrez, P., Pérez-Fígares, J.M., 2014. Structure and function of the ependymal barrier and diseases associated with ependyma disruption.

Jung, K.-H., Stephens, K.A., Yochim, K.M., Riphagen, J.M., Kim, C.M., Buckner, R.L., Salat, D.H., 2021. Heterogeneity of cerebral white matter lesions and clinical correlates in older adults. Stroke 52, 620–630.

Kaster, T., Sack, I., Samani, A., 2011. Measurement of the hyperelastic properties of ex vivo brain tissue slices. J. Biomech. 44, 1158–1163.

Khanra, S., Srivastava, N.K., Chail, V., Khess, C.R.J., 2016. Prevalence and characteristics of cavum septum pellucidum in schizophrenia: A 16 slice computed tomography study. Indian J. Psychol. Med. 38, 455–459.

Kim, S.H., Yun, C.H., Lee, S.Y., Choi, K.H., Kim, M.B., Park, H.K., 2012. Age-dependent association between cigarette smoking on white matter hyperintensities. Neurol. Sci. 33, 45–51.

Lambert, C., Benjamin, P., Zeestraten, E., Lawrence, A.J., Barrick, T.R., Markus, H.S., 2016. Longitudinal patterns of leukoaraiosis and brain atrophy in symptomatic small vessel disease. Brain 139, 1136–1151.

Lee, W.-J., Jung, K.-H., Ryu, Y.J., Kim, J.-M., Lee, S.-T., Chu, K., Kim, M., Lee, S.K., Roh, J.-K., 2018. Association of cardiac hemodynamic factors with severity of white matter hyperintensities in chronic valvular heart disease. JAMA Neurol. 75, 80–87.

Linninger, A.A., Tsakiris, C., Zhu, D.C., Xenos, M., Roycewicz, P., Danziger, Z., Penn, R., 2005. Pulsatile cerebrospinal fluid dynamics in the human brain. IEEE Trans. Biomed. Eng. 52, 557–565.

Luo, J., Shook, B.A., Daniels, S.B., Conover, J.C., 2008. Subventricular zone-mediated ependyma repair in the adult mammalian brain. J. Neurosci. 28, 3804–3813.

Maillard, P., Carmichael, O., Harvey, D., Fletcher, E., Reed, B., Mungas, D., DeCarli, C., 2013. Flair and diffusion mri signals are independent predictors of white matter hyperintensities. Am. J. Neuroradiol. 34, 54–61.

Maillard, P., Fletcher, E., Lockhart, S.N., Roach, A.E., Reed, B., Mungas, D., DeCarli, C., Carmichael, O.T., 2014. White matter hyperintensities and their penumbra lie along a continuum of injury in the aging brain. Stroke 45, 1721–1726.

Maniega, S.M., Hernández, M.C.V., Clayden, J.D., Royle, N.A., Murray, C., Morris, Z., Aribisala, B.S., Gow, A.J., Starr, J.M., Bastin, M.E., et al., 2015. White matter hyperintensities and normal-appearing white matter integrity in the aging brain. Neurobiol. Aging 36, 909–918.

Mayer, P.L., Kier, E.L., 1991. The controversy of the periventricular white matter circulation: a review of the anatomic literature. AJNR: Am. J. Neuroradiol. 12, 223.

Nunley, K.A., Ryan, C.M., Orchard, T.J., Aizenstein, H.J., Jennings, J.R., Ryan, J., Zgibor, J.C., Boudreau, R.M., Costacou, T., Maynard, J.D., Miller, R.G., Rosano, C., 2015. White matter hyperintensities in middle-aged adults with childhood-onset type 1 diabetes. Neurology 84, 2062–2069.

Oliver, C., González, C.A., Alvial, G., Flores, C.A., Rodríguez, E.M., Bátiz, L.F., 2013. Disruption of cdh2/n-cadherin-based adherens junctions leads to apoptosis of ependymal cells and denudation of brain ventricular walls. J. Neuropathol. Exp. Neurol. 72, 846–860.

Pena, A., Bolton, M.D., Whitehouse, H., Pickard, J.D., 1999. Effects of brain ventricular shape on periventricular biomechanics: a finite-element analysis. Neurosurgery 45, 107–118.

Quiñones-Hinojosa, A., Sanai, N., Soriano-Navarro, M., Gonzalez-Perez, O., Mirzadeh, Z., Gil-Perotin, S., Romero-Rodriguez, R., Berger, M.S., Garcia-Verdugo, J.M., Alvarez-Buylla, A., 2006. Cellular composition and cytoarchitecture of the adult human subventricular zone: a niche of neural stem cells. J. Comp. Neurol. 494, 415–434.

Raboel, P., Bartek, J., Andresen, M., Bellander, B., Romner, B., 2012. Intracranial pressure monitoring: invasive versus non-invasive methods—a review. Critical Care Res. Pract. 2012.

Reisberg, B., Ferris, S.H., de Leon, M., C.T., 1988. Global deterioration scale (GDS). Phychopharmacological Bull. 24, 661–663.

Roales-Buján, R., Páez, P., Guerra, M., Rodríguez, S., Vío, K., Ho-Plagaro, A., García-Bonilla, M., Rodríguez-Pérez, L.-M., Domínguez-Pinos, M.-D., Rodríguez, E.-M., et al., 2012. Astrocytes acquire morphological and functional characteristics of ependymal cells following disruption of ependyma in hydrocephalus. Acta Neuropathol. 124, 531–546.

Sachdev, P., Wen, W., Chen, X., Brodaty, H., 2007. Progression of white matter hyperintensities in elderly individuals over 3 years. Neurology 68, 214–222.

Sarnat, H.B., 1995. Ependymal reactions to injury. A review. J. Neuropathol. Exp. Neurol. 54, 1–15.

Scheltens, P., Barkhof, F., Leys, D., Wolters, E.C., Ravid, R., Kamphorst, W., 1995. Histopathologic correlates of white matter changes on mri in alzheimer's disease and normal aging. Neurology 45, 883–888.

Schmidt, R., Ropele, S., Enzinger, C., Petrovic, K., Smith, S., Schmidt, H., Matthews, P.M., Fazekas, F., 2005. White matter lesion progression, brain atrophy, and cognitive decline: the austrian stroke prevention study. Ann. Neurol.: Off. J. Am. Neurol. Assoc. Child Neurol. Soc. 58, 610–616.

Shook, B.A., Lennington, J.B., Acabchuk, R.L., Halling, M., Sun, Y., Peters, J., Wu, Q., Mahajan, A., Fellows, D.W., Conover, J.C., 2014. Ventriculomegaly associated with ependymal gliosis and declines in barrier integrity in the aging human and mouse brain. Aging Cell 13, 340–350.

Soellinger, M., Rutz, A.K., Kozerke, S., Boesiger, P., 2009. 3D cine displacement-encoded MRI of pulsatile brain motion. Magn. Reson. Med. 61, 153–162.

Terem, I., Ni, W.W., Goubran, M., Rahimi, M.S., Zaharchuk, G., Yeom, K.W., Moseley, M.E., Kurt, M., Holdsworth, S.J., 2018. Revealing sub-voxel motions of brain tissue using phase-based amplified MRI (aMRI). Magn. Reson. Med. 80, 2549–2559.

Todd, K.L., Brighton, T., Norton, E.S., Schick, S., Elkins, W., Pletnikova, O., Fortinsky, R.H., Troncoso, J.C., Molfese, P.J., Resnick, S.M., et al., 2018. Ventricular and periventricular anomalies in the aging and cognitively impaired brain. Front. Aging Neurosci. 9, 445.

Tombaugh, T.N., McIntyre, N.J., 1992. The mini-mental state examination: a comprehensive review. J. Am. Geriatr. Soc. 40, 922–935.

van Dommelen, J., van der Sande, T., Hrapko, M., Peters, G., 2010. Mechanical properties of brain tissue by indentation: Interregional variation. J. Mech. Behav. Biomed. Mater. 3, 158–166.

Van Leijsen, E.M., Bergkamp, M.I., Van Uden, I.W., Ghafoorian, M., Van Der Holst, H.M., Norris, D.G., Platel, B., Tuladhar, A.M., de Leeuw, F.-E., 2018. Progression of white matter hyperintensities preceded by heterogeneous decline of microstructural integrity. Stroke 49, 1386–1393.

Veeraval, L., O'Leary, C.J., Cooper, H.M., 2020. Adherens junctions: Guardians of cortical development. Front. Cell Dev. Biol. 6.

Visser, V.L., Rusinek, H., Weickenmeier, J., 2021. Peak ependymal cell stretch overlaps with the onset locations of periventricular white matter lesions. Sci. Rep. 11 (1), 1–12.

Wardlaw, J.M., Hernández, M.C.V., Munoz-Maniega, S., 2015. What are white matter hyperintensities made of? J. Am. Heart Assoc. 4, e001140.

Wardlaw, J., Sandercock, P., Dennis, M., Starr, J., 2003. Is breakdown of the blood–brain barrier responsible for lacunar stroke, leukoaraiosis, and dementia? Stroke 34, 806–812.

Weickenmeier, J., de Rooij, R., Budday, S., Steinmann, P., Ovaert, T., Kuhl, E., 2016. Brain stiffness increases with myelin content. Acta Biomater. 42, 265–272.

Zhong, X., Meyer, C.H., Schlesinger, D.J., Sheehan, J.P., Epstein, F.H., Larner, J.M., Benedict, S.H., Read, P.W., Sheng, K., Cai, J., 2009. Tracking brain motion during the cardiac cycle using spiral cine-DENSE MRI. Med. Phys. 36, 3413–3419.

Zhou, Z., Li, X., Kleiven, S., 2020. Biomechanics of periventricular injury. J. Neurotrauma 37, 1074–1090.

Zhu, D.C., Xenos, M., Linninger, A.A., Penn, R.D., 2006. Dynamics of lateral ventricle and cerebrospinal fluid in normal and hydrocephalic brains. J. Magn. Reson. Imaging 24, 756–770.